Anal Bioanal Chem (2007) 388:1583–1594
DOI 10.1007/s00216-007-1269-0

ORIGINAL PAPER

Computer simulations of a dielectric barrier discharge used for analytical spectrometry

Tom Martens · Annemie Bogaerts · Wouter Brok · Jan van Dijk

Received: 30 January 2007 / Revised: 17 March 2007 / Accepted: 19 March 2007 / Published online: 11 April 2007

Abstract A model developed for a dielectric barrier discharge (DBD) in helium, used as a new spectroscopic source in analytical chemistry, is presented in this paper. The model is based on the fluid approach and describes the behavior of electrons, He^+ and He_2^+ ions, He metastable atoms, He atoms in higher excited levels, and He_2 dimers. The He ground-state atoms are regarded as background gas. The characteristic effect of charging/discharging of the dielectrics which cover both electrodes is also simulated. Typical results of the model include the distribution of potential inside the plasma (and the potential drop across the dielectrics), the electric current and gap voltage as a function of time for a given applied potential profile, the spatial and temporal number-density profiles of the different plasma species, and the relative contributions of the mechanisms of their production and loss.

Keywords Dielectric barrier discharge · Computer simulations · Modeling · Microplasma

T. Martens · A. Bogaerts (✉)
Research Group PLASMANT,
Department of Chemistry,
University of Antwerp,
Universiteitsplein 1,
2610 Wilrijk-Antwerp, Belgium
e-mail: annemie.bogaerts@ua.ac.be

W. Brok · J. van Dijk
Department of Applied Physics,
Eindhoven University of Technology,
Den Dolech 2, Postbus 513, 5600 MB Eindhoven,
The Netherlands

Introduction

In recent years there has been increased interest in miniaturization of analytical instrumentation and methods, also called "lab-on-a-chip". In this respect, much attention has been devoted to miniaturized plasma sources. These so-called microplasmas have several advantages, including cheaper instruments and operation, because smaller amounts of sample and reagents are used. High-throughput measurements might also become possible if several plasmas are used in parallel. Finally, if the instrumentation can be made portable, it can be used outside the laboratory. Microplasmas exist in a variety of configurations, operating either at atmospheric or reduced pressure, for instance based on direct-current (dc) glow discharges used as molecular emission detectors [1–4], capacitively coupled radio-frequency (CCRF) discharges [5–10] including furnace atomization plasma excitation sources [11–16], microwave-induced plasmas based on the microstrip technology [17–19], miniature inductively coupled plasmas [20–22], electrolyte-as-cathode glow discharges (ELCAD) [23–27] and liquid-sampling atmospheric-pressure glow discharges (LS-APGD) [28–31], dielectric barrier discharges (DBDs) [32–36], microstructured electrode discharges (MSD) [34, 37, 38], and some other variations [39]. Several good review papers giving an overview and a description of these different types of analytical microplasma can be found in the literature [40–43]. Microplasmas in a variety of configurations are also of great interest for other than analytical spectrometry applications [44].

In the work discussed in this paper we investigated, by numerical simulation, the plasma characteristics of a microplasma, more specifically a DBD, as developed by Niemax and coworkers [32–35]. A DBD is typically formed between two parallel electrodes with a gap distance

of the order of 0.1–10 mm. Because one or both electrodes are covered with a dielectric barrier, the DBD cannot be operated with direct current (dc), because of dielectric charging issues. Typically they are operated with sinusoidal wave currents, square wave currents, or pulsed wave forms with a frequency ranging from a few Hz to MHz, usually in the kHz range [45]. The dielectric constant and thickness of the dielectric determine the amount of displacement current that can be passed through the dielectric. In most applications the dielectric limits the average current density in the gas space and guarantees that no spark or arc can occur in the discharge gap. DBDs are often operated at atmospheric pressure but are strongly non-equilibrium plasmas. They have unique features and characteristics which have provided the basis for a host of applications, for example ozone generation, gas treatment, excimer lamps, plasma display panels, and surface engineering, including cleaning, activation, and coating deposition [46–54].

Niemax and coworkers developed a DBD operating at reduced pressure (~10–180 mbar) and used it as a microchip source in analytical spectrometry [32–35]. This type of DBD was characterized by a dielectric layer on each electrode. It was shown to be a small, low-electric-power (<1 W), low-gas-temperature (~600 K) plasma source, with excellent dissociation capability for molecular species. It has been used in plasma modulation diode laser absorption spectrometry of excited chlorine and fluorine, with, typically, helium or argon as the plasma gas.

To obtain more insight into the plasma characteristics of the DBD we have developed a fluid model that describes the behavior of the different plasma species. In the next two sections this model will be explained in more detail. Typical calculation results will then be presented and a conclusion and outlook for future research will complete the paper.

Description of the model

The fluid model applied for this purpose was originally developed by Hagelaar for a DBD used in plasma display panels [55]. It was later transformed and extended by Brok and van Dijk, and integrated into their Plasimo code [56–59]. It consists of a set of continuity equations and flux equations, one of each for each type of species incorporated in the model. The model is applied here to a DBD in helium. The species included in the model are electrons, He^+ and He_2^+ ions, He ground-state atoms, He_2 dimers, He atoms excited to metastable levels (i.e. He(2^3S) and He (2^1S), combined into one level with a threshold energy of 19.82 eV; denoted He_m^*), and He atoms in higher excited levels, lumped together into one effective level with a threshold of 20.61 eV (denoted He**). This method of combining several levels into an effective level is commonly used in modeling to limit the complexity of the calculations, when the focus is on the general plasma characteristics rather than on the detailed behavior of the excited levels [60].

The continuity equations describe the production and loss of the different species:

$$\frac{\partial n_i}{\partial t} + \overline{\nabla} \bullet \overline{j_i} = R_{prod,i} - R_{loss,i}$$

where n, $\overline{j}$ and R denote species number density, flux, and production or loss rate and the index i refers to the different species. The flux equations describe transport based on diffusion and on migration in the electric field (for the charged species):

$$\overline{j_i} = \mu_i n_i \overline{E} - D_i \overline{\nabla} n_i$$

where E is the electric field, and μ and D denote the mobility and diffusion coefficient of the different species. Note that the mobility is taken as a positive value for the positive ions and a negative value for the electrons (and negative ions, if included in the model). For the neutral species, the first term is zero.

For the electrons an energy-balance equation is also solved, on the basis of energy gain from the electric field (first term on right-hand side) and energy changes because of collisions (second term on right-hand side):

$$\frac{\partial w_e}{\partial t} + \overline{\nabla} \bullet \overline{j_w} = -e\overline{j_e} \bullet \overline{E} + R_w$$

where $w_e = n_e \varepsilon_e$ is the electron energy density and j_w is the electron energy flux density, given by [61]:

$$\overline{j_w} = \frac{5}{3}\mu_e w_e \overline{E} - \frac{5}{3} D_e \overline{\nabla} w_e$$

Note that the energy changes are usually loss of energy (i.e. ionization and excitation) but gain of energy can occur as a result of superelastic collisions (e.g. reaction 5 of Table 1).

For the ions and neutral species no energy-balance equation needs be included, because these species can be regarded as being at the same energy (temperature) as the background gas. The gas temperature is assumed to be 300 K, uniformly distributed over the discharge. For these species, moreover, the local field approximation can be used, i.e. the mobility and diffusion coefficients of the heavy particles are taken to be functions of the local reduced electric field (local field divided by pressure). The values used are taken from Ref. [62].

Together with these continuity and flux equations and the electron-energy-balance equation the Poisson equation

Table 1 Overview of the different processes taken into account in the model

Reaction No.	Name	Reaction equation	Rate constant or cross-section	Ref.
1	Electron-impact excitation	$e^-+He \rightarrow e^-+He^*_m$	$\sigma(E)$	[64]
2	Electron-impact excitation	$e^-+He \rightarrow e^-+He^{**}$	$\sigma(E)$	[64]
3	Electron-impact ionization	$e^-+He \rightarrow 2\ e^-+He^+$	$\sigma(E)$	[64]
4	Electron-impact ionization	$e^-+He^*_m \rightarrow 2\ e^-+He^+$	$\sigma(E)$	[65]
5	Electron-impact de-excitation	$e^-+He^*_m \rightarrow e^-+He$	$k=2.9\times10^{-15}$ m^3 s^{-1}	[66, 67]
6	Electron-impact dissociation	$e^-+He_2 \rightarrow e^-+2\ He$	$k=3.8\times10^{-15}$ m^3 s^{-1}	[67]
7	Ion–electron recombination	$He^++2\ e^- \rightarrow He^*+e^-$	$k=6\times10^{-32}$ m^6 s^{-1}	[67]
8	Ion–electron dissociative recombination	$He_2^++2\ e^- \rightarrow He^*+He+e^-$	$k=2.8\times10^{-32}$ m^6 s^{-1}	[67]
9	Ion–electron dissociative recombination	$He_2^++e^-+He \rightarrow He^*+2\ He$	$k=3.5\times10^{-39}$ m^6 s^{-1}	[67]
10	Ion–electron recombination	$He_2^++2\ e^- \rightarrow He_2+e^-$	$k=1.2\times10^{-33}$ m^6 s^{-1}	[67]
11	Ion–electron recombination	$He_2^++e^-+He \rightarrow He_2+He$	$k=1.5\times10^{-39}$ m^6 s^{-1}	[67]
12	Hornbeck–Molnar associative ionization	$He^{**}+He \rightarrow He_2^++e^-$	$k=1.5\times10^{-17}$ m^3 s^{-1}	[60]
13	Metastable–metastable associative ionization	$He^*_m+He^*_m \rightarrow He_2^++e^-$	$k=2.03\times10^{-15}$ m^3 s^{-1}	[66, 67]
14	Metastable–metastable ionization	$He^*_m+He^*_m \rightarrow He^++He+e^-$	$k=8.7\times10^{-16}$ m^3 s^{-1}	[66, 67]
15	Ion conversion	$He^++2\ He \rightarrow He_2^++He$	$k=6.5\times10^{-44}$ m^6 s^{-1}	[67]
16	Metastable-induced association	$He^*_m+2\ He \rightarrow He_2+He$	$k=1.9\times10^{-46}$ m^6 s^{-1}	[67]
17	Metastable-induced dissociative ionization	$He^*_m+He_2 \rightarrow He^++2\ He+e^-$	$k=5\times10^{-16}$ m^3 s^{-1}	[67]
18	Metastable-induced ionization	$He^*_m+He_2 \rightarrow He_2^++He+e^-$	$k=2\times10^{-15}$ m^3 s^{-1}	[67]
19	Dimer-induced dissociative ionization	$He_2+He_2 \rightarrow He^++3\ He+e^-$	$k=3\times10^{-16}$ m^3 s^{-1}	[67]
20	Dimer-induced ionization	$He_2+He_2 \rightarrow He_2^++2\ He+e^-$	$k=1.2\times10^{-15}$ m^3 s^{-1}	[67]
21	He-atom-induced dissociation	$He_2+He \rightarrow 3\ He$	$k=4.9\times10^{-22}$ m^3 s^{-1}	[60]

The electron-impact ionization and excitation processes are treated with energy-dependent cross-sections, which are depicted in Fig. 1. The reactions between ions and/or neutral species, electron-impact de-excitation and dissociation, and electron–ion recombination reactions are described with a rate coefficient, which is also presented in the table. The references to the papers from where the cross-sections and rate coefficients were adopted are also included

is solved within the same time-step, to furnish a self-consistent electric field distribution:

$$\nabla^2 V = -\frac{e}{\varepsilon_0}\left[n_{He^+} + n_{He_2^+} - n_e\right]$$

The reactions taken into account in the model, which define the production and loss processes of the different species, are summarized in Table 1, with reference to the rate coefficients or cross-sections used. Note that for most of the electron-induced processes the reaction rates are calculated on the basis of energy-dependent cross-sections, and with a separate program, called BOLSIG+, which is based on a Boltzman equation [63]. In this program the exponential spatial growth model was used, as is recommended [63]. This program is applied for a wide range of different, fixed reduced electric fields. For each value of the reduced electric field the average electron energy, the mobility of the electrons, and the rates of the different electron-induced processes are tabulated. By use of these tables, the rates, mobilities, and diffusion coefficients (derived from the mobilities using the well-known Einstein relationship, assuming the bulk electrons are Maxwellian), will be applied; this corresponds to the electron energy calculated with the above electron-energy-balance equation.

The cross-sections of the electron-induced reactions are plotted as a function of electron energy in Fig. 1. Beside

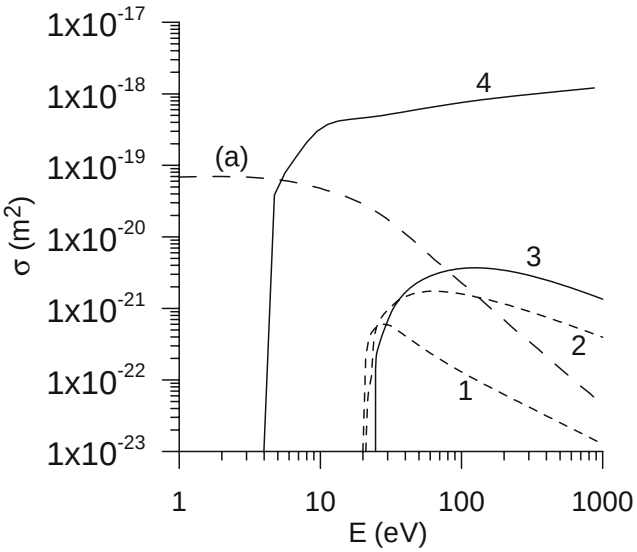

Fig. 1 Cross-sections of the different electron-induced processes as a function of electron energy. The *labels* correspond to the numbers in Table 1. (*1*) Electron-impact excitation to the He metastable levels He^*_m (*2*) Electron-impact excitation to the higher excited He levels (He**). (*3*) Electron-impact ionization from the He ground state. (*4*) Electron-impact ionization from the He metastable level. The *label (a)* denotes the electron elastic cross-section for He atoms, which is also included in the Boltzman model, but not in the fluid model, because it yields no production or loss of species. These cross-sections were adopted from Ref. [64] except for the cross-section of reaction 4, which originates from Ref. [65]

two electron-impact ionization reactions (solid lines) and two electron-impact excitation reactions (small dashed lines), the cross-section of the electron-induced elastic reaction is also plotted (large dashed line), because this reaction is also included in the Boltzman model. It is clear that the electron-impact excitation and ionization reactions from the He ground state have a lower value and a higher threshold energy than the electron-impact ionization reaction from the He_m^* level. The latter process, however, only occurs with He metastable atoms, which usually have a much lower number density in the plasma than the He ground-state atoms, so this process is not so important, despite the larger cross-section (see also the "Results" section).

For reactions between ions and/or neutral species, also called heavy particles, a rate coefficient is used in the model, because these species are assumed to be thermal (see above). The same applies to the electron-induced de-excitation and dissociation reactions (nos. 5 and 6 in Table 1) and the electron-ion recombination reactions (nos. 7–11), because such reactions occur with low-energy electrons. On the basis of the detailed report of Deloche et al. [67] dissociative He_2^+–electron recombination is included in the model as a three-body process, with either electrons or He atoms as the third bodies (reactions 8 and 9, respectively). We have, however, repeated our calculations using a simple two-body dissociative recombination reaction, with a rate constant of 10^{-14} m^3 s^{-1} [68] and this yielded the same results. In addition to dissociative recombination we have also included three-body non-dissociative electron–He_2^+ recombination giving rise to He_2 dimers. The other reactions included in the model are between heavy particles, and represent association, dissociation, (associative or dissociative) ionization, and ion conversion.

The model explained above seems very similar to the fluid models developed earlier by our group for gas discharge plasmas [69, 70]. There are, however, distinct differences for a fluid model for a gas discharge between two conducting electrodes. Indeed, the effect of the dielectrics covering the electrodes must be taken into account. The Poisson equation is, therefore, solved not only within the plasma but also inside the dielectrics, where it is reduced to:

$$\nabla^2 V = 0$$

because no species are present inside the dielectrics.

The effect of charge accumulation on the dielectric materials is also considered, by using Gauss's law:

$$\varepsilon_{\text{dielectric}} \overline{E}_{\text{dielectric}} \cdot \overline{u}_n - \varepsilon_{\text{gas}} \overline{E}_{\text{gas}} \cdot \overline{u}_n = \sigma$$

where $\overline{E}_{\text{dielectric}}$ and $\overline{E}_{\text{gas}}$ are the electric field inside the dielectric and in the gas discharge, respectively, $\overline{u}_n$ is the unit vector pointing normal to the wall where the charge accumulation occurs, and σ is the surface charge density on the dielectric, calculated from the charged particle flux directed to the surface.

The boundary conditions of the electrons are largely determined by secondary electron emission from the ions. Following the procedure of Hagelaar et al. for a plasma-addressed liquid-crystal (PALC) display cell with glass dielectric plates [71] we use a constant secondary-electron-emission coefficient of 0.2 for the helium ions and also consider that this ion-induced secondary-electron emission produces electrons with a mean initial energy of 5 eV. Reflection at the walls is neglected and electron desorption from the dielectrics is not considered, because it has been stated [72] that the latter process is very unlikely to happen.

The coupled differential equations are solved by the so-called "modified strongly implicit method", developed by Schneider and Zedan [73], and using an extra stabilization method, as explained elsewhere [55], until convergence is reached within every time-step of the periodic cycle, and periodic behavior over the discharge cycles is obtained.

Setup and conditions

The model was applied to the DBD described elsewhere [32]. It consisted of two flat glass plates, each with a 50-mm-long aluminium electrode. Both electrodes were covered by 20 μm-thick glass layers, i.e. the dielectric layers, as illustrated schematically in Fig. 2. The distance between the electrodes, including the dielectric layers, was 1 mm. A rectangular voltage pulse of 750 V (peak-to-peak) was applied at the powered electrode, with a rise-time of 2 μs, whereas the other electrode was grounded. The frequency is typically of the order of 5–20 kHz, and we used a value of 20 kHz. In the experiment the average power was very low, between 0.5 and 1 W. It has also been reported that any kind of noble gas at pressures between 10 and 180 mbar can be ignited and sustained. As mentioned in the section "Description of the model", we applied the model to a helium DBD, and the gas pressure and temperature chosen were 80 mbar and 300 K, respectively.

Results and discussion

Electrical characteristics

Figure 3 shows the applied potential as a function of time (dashed line), for typical conditions of 80 mbar He pressure, 20 kHz, and 750 V (peak-to-peak), the calculated

Fig. 2 Schematic diagram of the setup

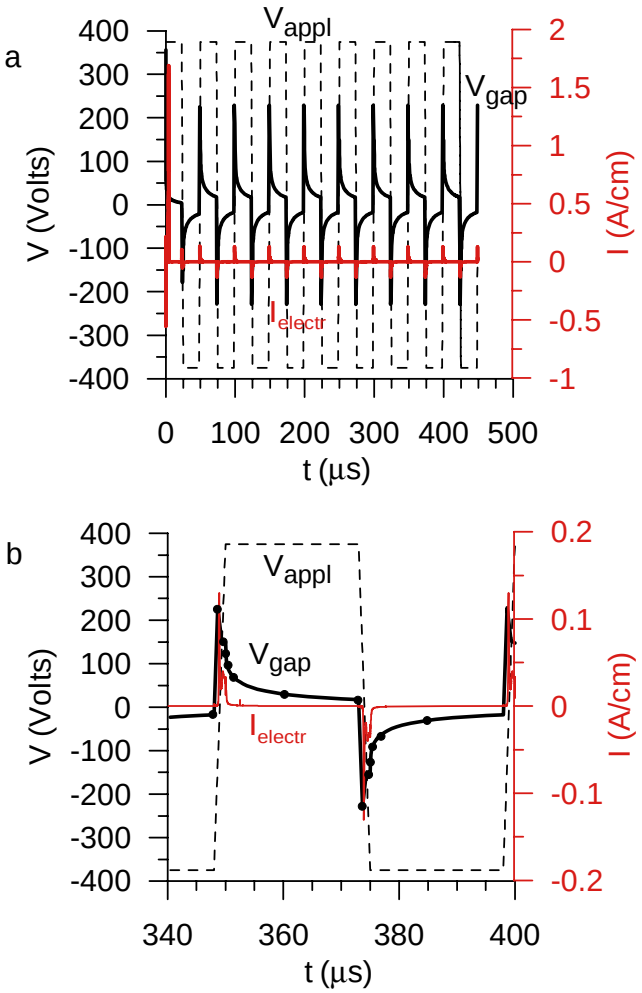

Fig. 3 Potential applied to the electrodes (V_{appl}, *black dashed line*, *left axis*) and calculated electric current density (*red line*, *right axis*), as a function of time, at 80 mbar, 20 kHz, and 750 V_{pp}. The calculated voltage over the discharge gap (so-called gap voltage, V_{gap}) is also plotted (*black solid line*, *left axis*), because this determines the plasma characteristics. (**a**) shows the temporal periodicity over a long time whereas (**b**) is a magnification of one period, consisting of a positive and a negative voltage polarity. In (**b**) the *solid circles* on the gap voltage profile denote specific moments in time, related to Fig. 4

electric current density (red line), and the calculated potential drop over the discharge gap (so-called gap voltage; solid black line). The latter arises as a result of the applied voltage and because of charging/discharging of the dielectrics. Indeed, the applied potential causes a rise in the gap voltage until breakdown is reached, which seems to occur at a gap voltage of 230 V. A plasma is formed, the discharge gas ionizes, and the charged particles migrate toward the electrode which bears an opposite charge. In this way charge accumulation occurs on the dielectric surface and the electric field in the discharge gap (or gap potential) diminishes, because it is the sum of the field induced by the applied potential and the opposite field created by the accumulated charges. This stabilizing effect makes DBDs so popular in producing controlled atmospheric pressure discharges, because it prevents formation of an arc [74].

Figure 3a shows the periodic behavior of voltage and current over a long time period and Fig. 3b focuses on one period, consisting of a positive and a negative potential polarity, to visualize the detailed behavior of voltage and current. Note that some points are marked at the gap voltage profile; this is related to the discussion given below in respect of Fig. 4.

Whereas the applied potential has an amplitude of 750 V (peak-to-peak, denoted V_{pp}), the resulting gap voltage has an amplitude of 460 V_{pp} during the applied voltage rise-time and decreases to approximately 40 V_{pp} during the plateau, before the powered electrode switches polarity. Note it is the gap voltage which determines the plasma characteristics. This is illustrated in the time-profile of the electric current density (red curve in Fig. 3) which peaks exactly at the peak of the gap voltage and drops to low values as soon as the applied potential reaches its steady-state value. This typical electric current profile is also found in experiments and simulations of the more frequently studied atmospheric pressure DBDs in helium [60, 75, 76].

Kunze et al. also measured the electric current in their DBD [33], although with argon as discharge gas. They also observed a peak, although the latter was somewhat wider than in our calculations. The width depends on the electrical circuit, however, for example the capacity of the electrode configuration. The operating conditions were also different, for example use of argon rather than helium as discharge gas, and different frequency (5 kHz rather than 20 kHz) and pressure (below 50 mbar rather than 80 mbar). It is reported in the literature that use of different discharge gases in DBDs gives rise to different plasmas, which have their own characteristic electric current profiles, some with wide current peaks (N_2 Townsend discharge) and some with narrow current peaks (He glow discharge) [77–80]. Moreover, a discharge cannot always be ignited in every type of discharge gas under similar electrical conditions. The properties of argon discharges in dielectric barrier configurations have not yet been subjected to such extensive studies as for He or N_2 discharges, so comparison is much more difficult. In our model we assumed a pure He discharge yet in the experiments gas impurities are always present and it is recognized that the presence of these impurities can lead to alteration of the electrical characteristics of the discharge [76, 81]. Exact comparison is, therefore, not possible, but at least the characteristic behavior of rise and extinguishing of the electric current, which is typical of DBDs, is found in our calculation results.

The potential drop across the electrodes is depicted in Fig. 4, at several moments in time, as indicated in the legend. Figure 4a (left; solid lines) illustrates the situation just before and during the positive applied potential polarity

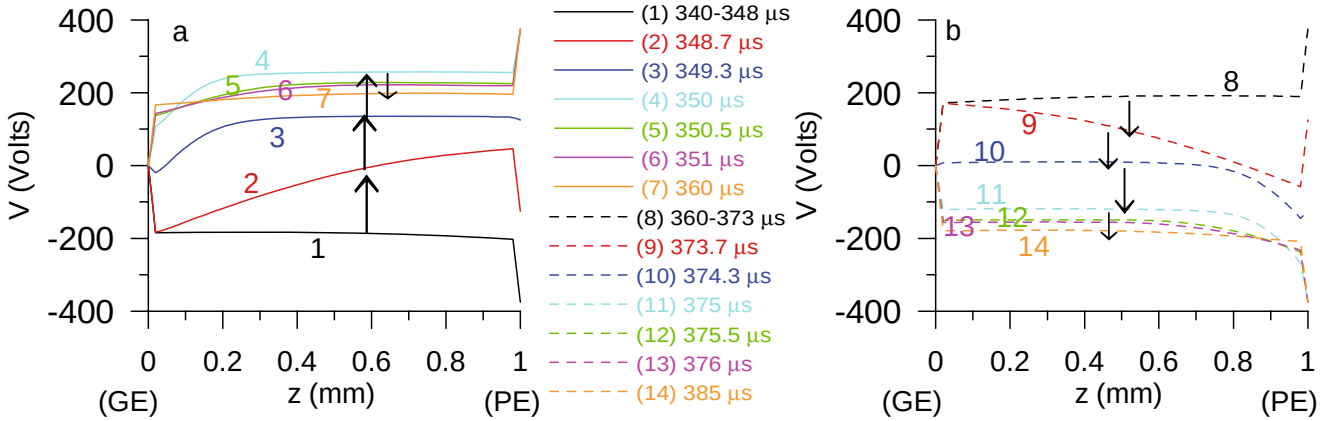

Fig. 4 Calculated voltage drop, or potential distribution, between the electrodes at several moments in time (*legend*), both when the powered electrode is negative (**a**, *solid lines*) and positive (**b**, *dashed lines*) under the same discharge conditions as in Fig. 3. The *arrows* represent the time evolution of the potential distribution. The positions of grounded electrode (*GE*) and powered electrode (*PE*) are also indicated. Note that not only the potential distribution inside the plasma but also the potential drop across the dielectrics is depicted

whereas Fig. 4b (right; dashed lines) refers to the situation when the applied potential polarity is (or will soon become) negative. These time-moments are also marked on the gap voltage profile of Fig. 3. The grounded and powered electrodes (GE, PE) are situated at the left and right borders, respectively, of Fig. 4. To explain the gap potential drop, or potential distribution inside the plasma, on the basis of the applied potential, the voltage drop across both dielectrics is also included in the figure. Note that the electrodes are separated from each other by a distance of 1 mm; both dielectrics have a thickness of 20 µm, hence the total discharge gap is 960 µm or 0.96 mm.

From Fig. 4a it is clear the potential distribution is constant in time from 340 µs to 348 µs, i.e. when the applied voltage is still negative. The grounded electrode (left) is at 0 V, and the powered electrode (right) is at −375 V. This voltage drops almost completely, however, in the dielectrics adjacent to the left and right electrodes. Indeed, the potential drop over these two dielectrics is approximately −180 V (each) whereas the potential drop over the plasma (so-called gap potential) is only approximately −20 V. This is also clear from Fig. 3b (solid black line).

As soon as the applied potential starts changing polarity, however, the potential distribution changes drastically, as visualized by the red, blue and cyan curves in Fig. 4a. After 348.7 µs (red curve) the applied voltage is only −125 V but the potential drops across both dielectrics are still approximately −180 V; hence the potential drop (or, better, increase) across the discharge is now approximately +230 V. This value corresponds to the maximum value of the gap potential reached as a function of time, as is also apparent from Fig. 3(b). Consequently, at this moment, the electric current also reaches its maximum (Fig. 3b).

After 349.3 µs (blue line) the applied potential is +125 V and the potential drop across the electrodes is very small (approx. 10–20 V), because of the process of discharging. The surface charges on the dielectrics (not shown here) also switch polarity, albeit about a microsecond later than the applied voltage. During the switching of the applied voltage and after a slight delay, therefore, a smaller potential drop across the dielectrics is seen. Hence, the gap potential at that time is approximately +150 V. At this moment, the potential distribution inside the plasma mostly resembles that of a direct current glow discharge in which the potential is almost constant and slightly above the potential of the most positive electrode (here at the right) in the largest part of the discharge, called the bulk plasma or negative glow, and drops strongly in front of the most negative electrode, characterizing the sheath or cathode dark space.

After 350 µs (cyan curve), the potential distribution inside the plasma has the same shape as that at 349.3 µs, and the total gap potential is again approximately +150 V. Now the applied potential has reached its (positive-polarity steady) value of +375 V, however, hence the remaining potential drop is now again found across both dielectrics (approx. 100–120 V each).

At later times, until 373 µs, the applied potential remains constant at +375 V but the potential drop across both dielectrics increases slightly, so the gap potential gradually decreases, as is clear from the green, pink, and orange curves in Fig. 4a, and from Fig. 3b. This situation corresponds also to the black dashed curve (representing 373 µs) in Fig. 4b.

After 373.7 µs, however, the applied potential starts to decrease again, to change polarity. At this moment there is still a large potential drop across the dielectrics, so the gap potential reaches its maximum negative value (i.e. −230 V; red dashed curve). After 374.3 µs the applied potential has become slightly negative (−125 V), the drop over the dielectrics is very small (because of the process of discharging as a result of the large electric current), and the gap voltage is still significant (approx. −150 V; blue dashed line). After 375 µs, and later, the applied potential

has reached its steady negative polarity of −375 V and the potential drop across the dielectrics starts to increase again, and so the gap potential gradually starts to decrease again as a function of time (or, better, become less negative), as is also found in Fig. 3b.

Note that the orange dashed curve in Fig. 4b coincides more or less with the black solid curve in Fig. 4a, so the cycle can be repeated when the applied potential starts changing polarity again. Note also that the second half period (Fig. 4b) is approximately the mirror image of the first half period (Fig. 4a), because of the symmetrical electrode configuration. To summarize, the arrows in Fig. 4a and b visualize the time evolution of the potential distributions.

Densities of the plasma species

Figure 5 illustrates the number density profiles of the electrons at different times corresponding approximately to the same times as in Fig. 4 and under the same discharge conditions as in Fig. 3. Note the logarithmic scale of this *y*-axis, which was necessary to fit all the curves on one plot.

After 348 μs (black solid line in Fig. 5a), i.e. just before the applied potential changes polarity and the gap voltage and electric current start to rise, the electron density is a few times 10^{14} m^{-3}; the profile is asymmetric and reaches its highest value near the grounded electrode (which is the more positive electrode at this time; cf. Fig. 4a).

As soon as the applied potential starts changing polarity the electron-density profile changes drastically. After 348.7 μs (red solid curve in Fig. 5a) the absolute values of the electron density are still approximately the same, but the maximum shifts completely toward the other (i.e. powered) electrode. After 349.3 μs (blue solid curve in Fig. 5a) the electron density has increased dramatically by almost three orders of magnitude, to values of a few times 10^{17} m^{-3} and the maximum is more spread over the entire discharge gap.

After this time the electron density starts to decay again, as is visualized by the cyan and green solid curves in Fig. 5a, and the profile becomes again more asymmetric, with its maximum near the powered electrode. The density profile shown after 361 μs (green solid curve in Fig. 5a) is more or less retained until 373 μs, symbolized by the black dashed curve in Fig. 5b.

At 373.7 μs the applied potential starts changing polarity and the electron density again changes drastically, with first a shift toward the other (grounded) electrode (red dashed line in Fig. 5b), followed by a dramatic increase and spreading of the maximum over the entire gap after 374.3 μs (blue dashed curve) and then, again, a decay and more asymmetric profiles after still later times (cyan and green dashed curves). The green dashed curve in Fig. 5b again coincides more or less with the black solid curve in Fig. 5a, illustrating that the cycle is repeated when the applied voltage again switches polarity.

The spatially averaged electron density is plotted as a function of time in Fig. 6 (red curve), with the spatially averaged densities of the other plasma species, for the same operating conditions as in the previous figures. As was already illustrated in Fig. 5, the electron density increases sharply after 349 μs, i.e. when the applied potential is switching polarity and the electric current reaches its maximum. After this (spatially averaged) maximum value of 5×10^{17} m^{-3} is achieved the density decays rapidly to values of the order of 10^{15} m^{-3} in approximately 5 μs, and then more slowly to values of the order of 10^{14} m^{-3}, before it starts to increase again when the applied voltage switches polarity.

The spatially averaged densities of the He^+ and He_2^+ ions (black and blue curves, respectively) have profiles similar to those of the electron density. Their (spatially averaged) maximum values are calculated to be 2.3×10^{17} and 4.2×10^{17} m^{-3}, respectively.

The neutral plasma species have different time profiles. The He metastable (He_m^*) density (cyan curve; ten times

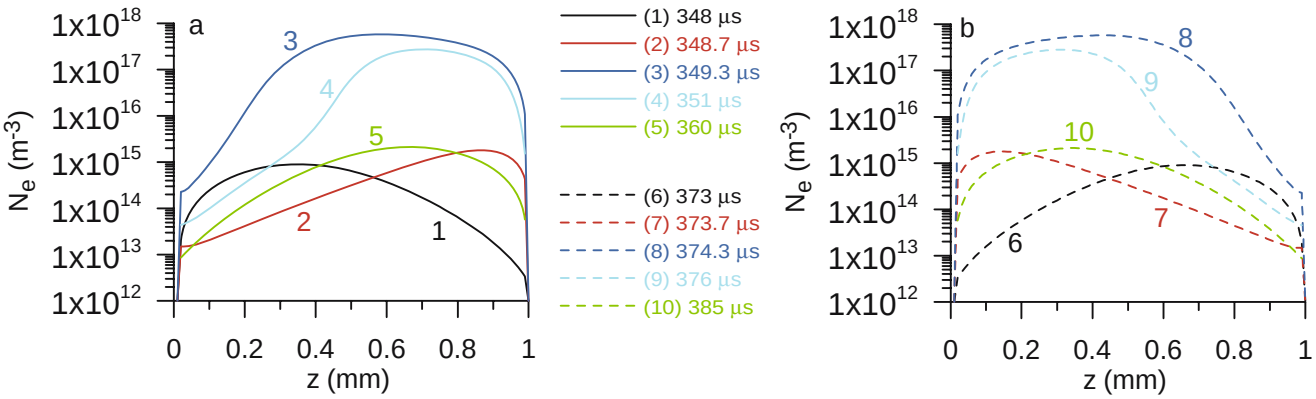

Fig. 5 Calculated electron number density profiles inside the plasma, at approximately the same moments in time as in Fig. 4, and under the same discharge conditions. Note the logarithmic scale of the *y*-axis, which was necessary to visualize all curves on one plot

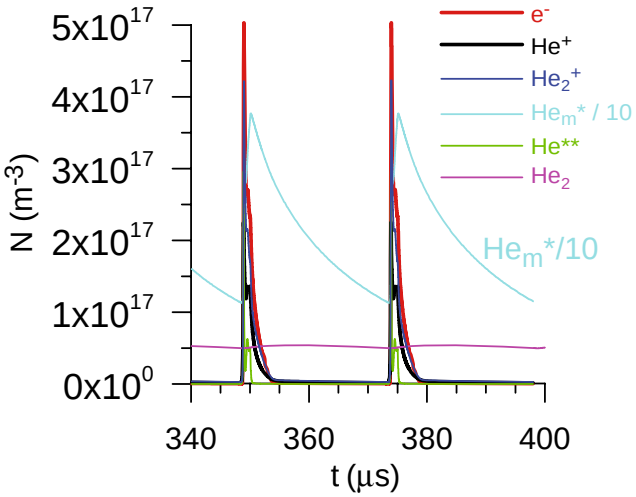

Fig. 6 Calculated spatially averaged number densities of the different plasma species as a function of time, under the same conditions as in Fig. 3. Note that the He_m^* density was divided by 10, to enable its inclusion in the same figure as the other curves

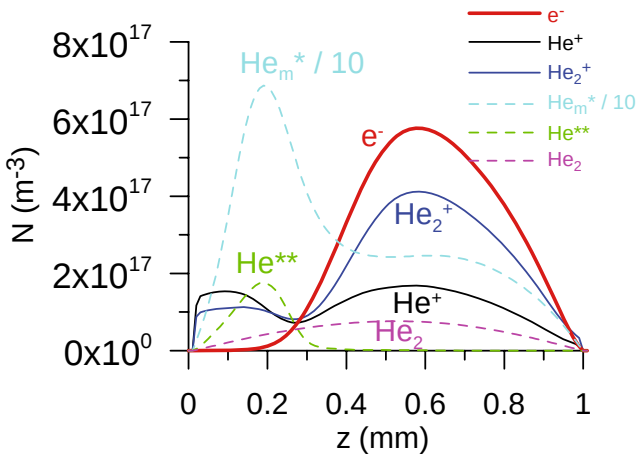

Fig. 7 Calculated number-density profiles of the different plasma species, at the peak of their temporal evolution (i.e. at 349 μs), for the same discharge conditions as in Fig. 3. The charged particles are represented with *solid lines* whereas the *dashed curves* stand for the neutral species. Note that the He_m^* density was divided by 10, to enable its inclusion in the same figure as the other curves

reduced to fit in the same plot) also increases sharply when the electron density reaches its maximum but it decays very slowly before it starts rising again when the potential switches polarity. The (spatially averaged) maximum is approximately 3.7×10^{18} m^{-3}, and the minimum value is still above 10^{18} m^{-3}. This slow decay illustrates that the metastables have a longer lifetime than the charged plasma species. Note that the density of these He_m^* atoms is approximately an order of magnitude higher than the densities of the other plasma species. Their density is, however, still about six orders of magnitude below the He ground-state atom density (which is approx. 10^{24} m^{-3} under the conditions studied).

The He atoms excited to higher levels (He**; green curve), on the other hand, are characterized by a much faster drop and, moreover, they have a very low density, with a (spatially averaged) maximum of only 5×10^{16} m^{-3}. Hence, they are clearly less important in the plasma than the He_m^* metastable atoms.

Finally, the He_2 dimers (pink curve) are characterized by a nearly constant density (~5×10^{16} m^{-3}) throughout time and are, hence, almost unaffected by the switches of applied potential polarity. Their density is the lowest of all the plasma species included. They can, however, become more important when the gas pressure increases, as is commonly the case for He DBDs used for technological applications [60, 66].

The spatial density profiles of these plasma species, plotted at 349 μs (i.e. when they reach their maximum density as a function of time) are illustrated in Fig. 7. The charged species are represented by solid lines and the neutral species by dashed lines. The electron density (red solid line) has a typical profile, which is also more or less characteristic of a dc glow discharge between conducting electrodes, with low values in the sheath near the cathode and much higher values in the bulk plasma. Note that this density profile is obtained after 349 μs, when the potential distribution was indeed found to resemble that of a dc glow discharge (blue line of Fig. 4a). At other moments in time the potential distribution and hence the electron density profile behave differently (Fig. 5).

The He^+ and He_2^+ ion densities (black and blue curves, respectively) also reach a maximum in the so-called bulk plasma, where the electrons reach their maximum density, but they are also characterized by a second maximum in the sheath near the grounded (i.e. most negative) electrode. For the He^+ ions this maximum is even slightly higher than the maximum in the bulk plasma. This illustrates that the plasma only resembles a dc glow discharge (at this time-moment) but is still different. At other times, moreover, there is a clear distinction from the behavior in a dc glow discharge (Figs. 4 and 5).

The He_m^* and He** density profiles (cyan and green dashed lines, respectively) also reach a maximum in the sheath, because they are predominantly formed by electron-impact excitation (see below), which is mainly important in this region, because here the electrons can gain sufficient energy from the electric field. Note that the He_m^* density profile is reduced by a factor of 10 to fit in the same figure. The density of excited He_m^* atoms (~7×10^{18} m^{-3} at the maximum of the profile) is, therefore, a factor of 40 higher than that of He** (~1.8×10^{17} m^{-3}).

The density of He_2 dimers is still lower, approximately 7.6×10^{16} m^{-3}, but they are more uniformly distributed throughout the discharge gap (pink curve).

Table 2 Calculated relative contributions of the different production and loss processes, for each of the different plasma species, both at the peak (i.e. 349 μs) and during the plateau time (i.e. 360 μs), at the same discharge conditions as indicated in Fig. 3

Process	Relative contribution (%)	
	At peak (349 μs)	During plateau (360 μs)
Production of electrons		
(3) Electron-impact ionization from He ground state	39.3	0.1
(4) Electron-impact ionization from metastables	2.5	2.2
(12) Hornbeck–Molnar associative ionization	58.2	1.64
(13) Metastable–metastable associative ionization	0.07	65.7
(14) Metastable–metastable ionization	0.03	28.1
(17) Metastable-induced dissociative ionization of He_2	~0	0.4
(18) Metastable-induced ionization of He_2	0.002	1.8
(19) Dimer-induced dissociative ionization of He_2	~0	0.008
(20) Dimer-induced ionization of He_2	~0	0.03
Loss of electrons		
(7) He^+ ion–electron recombination	44.7	0.6
(8) He_2^+ dissociative recombination with e^- as third body	35.8	0.5
(9) He_2^+ dissociative recombination with He as third body	12.6	69.3
(10) He_2^+ recombination with e^- as third body	1.5	0.02
(11) He_2^+ recombination with He as third body	5.4	29.6
Production of He^+ ions		
(3) Electron-impact ionization from He ground state	94	6.9
(4) Electron-impact ionization from metastables	5.9	0.3
(14) Metastable–metastable ionization	0.07	91.3
(17) Metastable-induced dissociative ionization of He_2	~0	1.5
(19) Dimer-induced dissociative ionization of He_2	~0	0.03
Loss of He^+ ions		
(7) Ion–electron recombination	94	~100
(15) He^+ to He_2^+ ion conversion	6	~0
Production of He_2^+ ions		
(12) Hornbeck–Molnar associative ionization	99.3	2.2
(13) Metastable–metastable associative ionization	0.1	88.8
(15) He^+ to He_2^+ ion conversion	0.6	6.5
(18) Metastable-induced ionization of He_2	0.003	2.4
(20) Dimer-induced ionization of He_2	0.004	0.04
Loss of He_2^+ ions		
(8) Dissociative recombination with e^- as third body	64.7	0.5
(9) Dissociative recombination with He as third body	22.7	69.7
(10) Ion–electron recombination with e^- as third body	2.8	0.02
(11) Ion–electron recombination with He as third body	9.8	29.8
Production of He_m^* metastable atoms		
(1) Electron-impact excitation	99.9	~100
(7) He^+–electron recombination	0.03	~0
(8) He_2^+–electron dissociative recombination with e^- as third body	0.02	~0
(9) He_2^+–electron dissociative recombination with He as third body	0.008	0.002
Loss of He_m^* metastable atoms		
(4) Electron-impact ionization	94.9	2.0
(5) Electron-impact de-excitation	0.7	9.2
(13) Metastable–metastable associative ionization	2.7	60.7
(14) Metastable–metastable ionization	1.2	26.0
(16) Metastable-induced association	0.4	9.2
(17) Metastable-induced dissociative ionization of He_2	0.02	0.4
(18) Metastable-induced ionization of He_2	0.06	1.7
Production of He** atoms		
(2) Electron-impact excitation	100	100

Table 2 (continued)

Process	Relative contribution (%)	
	At peak (349 μs)	During plateau (360 μs)
Loss of He** atoms		
(12) Hornbeck–Molnar associative ionization	100	100
Production of He_2 dimers		
(10) He_2^+ ion–electron recombination with e^- as third body	5.9	~0
(11) He_2^+ ion–electron recombination with He as third body	20.9	~0
(16) Metastable-induced association	73.2	~100
Loss of He_2 dimers		
(6) Electron-impact dissociation	19.4	0.06
(17) Metastable-induced dissociative ionization	13.6	16.9
(18) Metastable-induced ionization	54.7	67.7
(19) Dimer-induced dissociative ionization	0.2	0.3
(20) Dimer-induced ionization	0.9	1.1
(21) He atom-induced dissociation	11.3	13.9

Importance of the production and loss processes of the different species

The characteristic temporal and spatial density profiles of the different plasma species can be explained by studying their production and loss mechanisms. It was found that all the electron-related processes (i.e. electron-impact reactions (1–6 in Table 1) and electron–ion recombination reactions (7–11 in Table 1)), and Hornbeck–Molnar associative ionization (reaction 11) and ion conversion (reaction 15) give a strong and narrow peak at approximately 349 μs. The He_m^* metastable-induced reactions (13, 14, 16–18 in Table 1) are, in contrast, characterized by a strong increase at 349 μs but a slow decay, similar to the He_m^* density behavior (Fig. 6). Finally, the He_2 dimer-induced reactions (19–21 in Table 1) seem to be nearly time-independent, in correlation with He_2 density behavior.

The calculated relative contributions of the different production and loss processes for the various species, obtained both at their peak density (349 μs), and during the plateau of the gap voltage (at 360 μs) are summarized in Table 2. The results for the peak and plateau of the opposite polarity are not given, because they were found to be exactly the same. The electrons are primarily formed from He ground-state atoms, by electron-impact ionization, and, at the peak of their density, by Hornbeck–Molnar associative ionization, whereas metastable–metastable (associative and normal) ionization is the most important production mechanism during the plateau. Indeed, by that time the electron density has already dropped to low values whereas the density of He_m^* metastable atoms is still substantial (Fig. 5). As far as loss of electrons is concerned, recombination with He^+ ions and dissociative recombination with He_2^+ ions seem to be nearly equally important processes at the peak. During the plateau both dissociative and normal recombination with He_2^+ ions were calculated to be the main loss mechanisms, but with He atoms as third body, because the electron density has dropped to low values, making these species less important as a third body.

The He^+ ions are mainly created from the He ground state, by electron-impact ionization, at the peak and by metastable–metastable ionization during the plateau. They are predominantly lost by electron–ion recombination. He^+ to He_2^+ ion conversion seems to be of minor importance, especially during the plateau.

Hornbeck–Molnar associative ionization was found to be the dominant mechanism of production of the He_2^+ ions at the peak whereas during the plateau time metastable–metastable ionization was most important. This is expected, because the He_m^* metastables are characterized by a much longer lifetime than the highly excited He** atoms. Loss of He_2^+ ions occurs mostly by dissociative recombination at the peak and by dissociative or normal recombination, but with He atoms as a third body, during the plateau time, by analogy with the loss mechanisms for the electrons.

The He_m^* atoms are almost exclusively produced by electron-impact excitation, both at the peak and during the plateau. The dominant mechanism of loss of these species is electron-impact ionization at the peak and metastable–metastable (associative or normal) ionization during the plateau. This again is expected, because the density of electrons is much higher and can more easily give rise to electron-induced processes at the peak whereas the density of metastables is still substantial during the plateau.

The He** atoms are formed by electron-impact excitation only, and are destroyed by Hornbeck–Molnar associative ionization, both at the peak and during the plateau, because these are the only production and loss mechanisms

included in the model for these species. Note that this is an approximation, because radiative decay will in reality also be responsible for loss of the He** atoms. To describe this accurately, however, different He** atomic levels would have to be considered separately in a type of collisional–radiative model [82], and this is beyond the scope of this study. The density of the He** atoms would, in any event, be much less than, for example, that of He_m^* metastable atoms, so they would not be very important under the conditions studied.

Finally, the He_2 dimers are predominantly produced by metastable induced association; at the peak of the densities, however, He_2^+ ion–electron recombination is also important, especially with He atoms as a third body. Loss of the He_2 dimers occurs mainly by metastable induced (dissociative) ionization and, to a lesser extent by He atom-induced dissociation. Electron-impact dissociation seems to be important only at the peak of its density, which again is expected, because of the rapid decay of electrons as a function of time.

Conclusion

We have presented results of a fluid model developed for a dielectric barrier discharge (DBD) in helium, used as a new source in analytical spectrochemistry. The model describes the behavior of electrons, He^+ and He_2^+ ions, He metastable atoms $\left(He_m^*\right)$, He atoms at highly excited levels (He**), and He_2 dimers. Characteristic of a DBD is that one or both electrodes are covered with dielectrics, which substantially affects the electrical behavior of the DBD. Indeed, the potential difference applied between the electrodes, drops not only inside the plasma, but also across the dielectrics, so the so-called gap potential (or potential difference across the plasma) is clearly different from the applied potential. It is the gap potential which determines the plasma characteristics. Consequently, the electric current profile follows the gap voltage profile more closely than it follows the applied voltage profile.

In addition to the electrical characteristics and the potential distribution inside the plasma as a function of time, the model also calculates the spatial and temporal number-density profiles of the different plasma species. It is found that, in addition to the He ground-state atoms, He atoms at metastable levels $\left(He_m^*\right)$ are the plasma species with the highest number density (at least an order of magnitude higher than the densities of the other plasma species). The temporal behavior of the He_m^* atoms is also different from that of the other plasma species. Indeed, the electrons, ions, and highly excited He** atoms reach a maximum density when the applied potential switches polarity, and their density drops again rapidly as a function of time. The density of metastable He_m^* atoms, on the other hand, decays very slowly as a function of time. Finally, the density of the He_2 dimers seems to be roughly time-independent, and they are of less importance than the other plasma species. This situation will change when the DBD is operated at much higher (e.g. atmospheric) pressure.

The relative contributions of the different production and loss mechanisms of the different plasma species were also determined, both at the peak of their densities (i.e. when the applied potential switches polarity) and during the plateau time of the applied voltage profile. It is illustrated that different production and loss mechanisms can become dominant at different moments in time.

In future work we would like to extend this model to other discharge gases (for example argon) and also to perform a detailed study on the effect of pressure, power, frequency, and gap width, to determine the optimum operating conditions for the analytical DBD and to assist experimental studies with this new type of plasma source.

References

1. Eijkel JCT, Stoeri H, Manz A (2000) J Anal At Spectrom 15:297–300
2. Eijkel JCT, Stoeri H, Manz A (2000) Anal Chem 72:2547–2552
3. Kim HJ, Woo YA, Kang JS, Anderson SS, Piepmeier EH (2000) Microchim Acta 134:1–7
4. Bessoth FG, Naji OP, Eijkel JCT, Manz A (2002) J Anal At Spectrom 17:794–799
5. Liang D, Blades MW (1989) Spectrochim Acta B 44:1049
6. Blades MW (1994) Spectrochim Acta B 49:47
7. Anghel SD, Frentiu T, Cordos EA, Simon A, Popescu A (1999) J Anal At Spectrom 14:541–545
8. Lu SY, LeBlanc CW, Blades MW (2001) J Anal At Spectrom 16:256–262
9. Bass A, Chevalier C, Blades MW (2001) J Anal At Spectrom 16:919–921
10. Yoshiki H, Horiike Y (2001) Jpn J Appl Phys 40:L360–L362
11. Sturgeon RE, Luong VT, Willie SN, Marcus RK (1993) Spectrochim Acta B 48:893–908
12. Pavski V, Chakrabarti CL, Sturgeon RE (1994) J Anal At Spectrom 9:1399–1409
13. Sturgeon RE, Guevremont R (1998) J Anal At Spectrom 13:229–233
14. Sun F, Sturgeon RE (1999) J Anal At Spectrom 14:901–912
15. Sun F, Sturgeon RE (1999) Spectrochim Acta B 54:2121–2141
16. Guevremont R, Sturgeon RE (2000) 15:37–42
17. Bilgic AM, Voges E, Engel U, Broekaert JAC (2000) J Anal At Spectrom 15:579–580
18. Bilgic AM, Engel U, Voges E, Kückelheim M, Broekaert JAC (2000) Plasma Sources Sci Technol 9:1–4
19. Hopwood J, Iza F (2004) J Anal At Spectrom 19:1145–1150
20. Yin Y, Messier J, Hopwood JA (1999) IEEE Trans Plasma Sci 27:1516–1524
21. Hopwood JA (2000) J Microelectromech Syst 9:309–313
22. Iza F, Hopwood J (2002) Plasma Sources Sci Technol 11:229–235
23. Cserfalvi T, Mezei P, Apai P (1993) J Phys D 26:2184–2188
24. Mezei P, Cserfalvi T, Janossy M (1997) J Anal At Spectrom 12:1203–1208
25. Mezei P, Cserfalvi T, Janossy M, Szöcs, Kim HJ (1998) J Phys D 31:2818–2825

26. Cserfalvi T, Mezei P (2003) J Anal At Spectrom 18:596–602
27. Kim HJ, Lee JH, Kim MY, Cserfalvi T, Mezei P (2000) Spectrochim Acta B 55:823–831
28. Davis WC, Marcus RK (2001) J Anal At Spectrom 16:931–937
29. Marcus RK, Davis WC (2001) Anal Chem 73:2903–2910
30. Davis WC, Marcus RK (2002) Spectrochim Acta B 57:1473–1486
31. Webb MR, Andrade FJ, Gamez G, McCrindle R, Hieftje GM (2005) 20:1218–1225
32. Miclea M, Kunze K, Musa G, Franzke J, Niemax K (2001) Spectrochim Acta B 56:37–43
33. Kunze K, Miclea M, Musa G, Franzke J, Vadla C, Niemax K (2002) Spectrochim Acta B 57:137–146
34. Miclea M, Kunze K, Franzke J, Niemax K (2002) Spectrochim Acta B 57:1585–1592
35. Kunze K, Miclea M, Franzke J, Niemax K (2003) Spectrochim Acta B 58:1435–1443
36. Zhu Z, Zhang S, Xue J, Zhang X (2006) Spectrochim Acta B 61:916–921
37. Franzke J, Kunze K, Miclea M, Niemax K (2003) J Anal At Spectrom 18:802–807
38. Penache C, Miclea M, Bräning-Demian A, Hohn O, Schössler S, Jahnke T, Niemax K, Schmidt-Böcking H (2002) Plasma Sources Sci Technol 11:476–483
39. Skelton RJ Jr, Chang H-CK, Farnsworth PB, Markides KE, Lee ML (1989) Anal Chem 61:2292–2298
40. Broekaert JAC (2002) Anal Bioanal Chem 374:182–187
41. Franzke J, Kunze K, Miclea M, Niemax K (2003) J Anal At Spectrom 18:802–807
42. Karanassios (2004) Spectrochim Acta B 59:909–928
43. Broekaert JAC, Siemens V (2004) Anal Bioanal Chem 380:185–189
44. Becker KH, Schoenbach KH, Eden JG (2006) J Phys D 39:R55–R70
45. Roth JR (1995) Industrial plasma engineering, vol 1: principles. IOP, Philadelphia
46. Kogelschatz U, Eliasson B, Egli W (1999) Pure Appl Chem 71:1819–1828
47. Sobel A (1991) IEEE Trans Plasma Sci 19:1032–1047
48. Kogelschatz U, Eliasson B, Hirth M (1988) Ozone: Sci Eng 10:367–377
49. Eliasson B, Kogelschatz U (1988) Appl Phys B 46:299–303
50. Penetrante BM, Brusasco RM, Merritt BT, Vogtlin GE (1999) Pure Appl Chem 71:1829–1835
51. Penetrante BM, Hsiao MC, Bardsley JN, Merritt BT, Vogtlin GE, Kuthi A, Burkhart CP, Bayless JR (1997) Plasma Sources Sci Technol 6:251–259
52. Borcial G, Anderson CA, Brown NMD (2003) Plasma Sources Sci Technol 12:335–344
53. Hubiccka Z, Cad M, Sicha M, Churpita A, Pokorný P, Soukup L, Jastrabik L (2002) Plasma Sources Sci Technol 11:195–202
54. Goossens O, Dekempeneer E, Vangeneugden D, Van de Leesta R (2001) Surf Coat Technol 142/144:474–481
55. Hagelaar G, Modeling of Microdischarges for Display Technology, PhD Dissertation, Eindhoven University of Technology, 2000
56. Brok WJM, van Dijk J, Bowden MD, van der Mullen JJAM, Kroesen GMW (2003) J Phys D: Appl Phys 36:1967–1979
57. Brok WJM, Bowden MD, van Dijk J, van der Mullen JJAM, Kroesen GMW (2005) J Appl Phys 98:013302
58. Wagenaars E, Brandenburg R, Brok WJM, Bowden MD, Wagner H-E (2006) J Phys D: Appl Phys 39:700–711
59. Brok WJM, Gendre MF, van der Mullen JJAM (2006) J Phys D: Appl Phys 40:156–162
60. Golubovskii YB, Maiorov VA, Behnke J, Behnke JF (2003) J Phys D 36:39–49
61. Raizer YP (1991) Gas discharge physics. Springer, Berlin Heidelberg New York
62. Ellis HW, Pai RY, McDaniel EW (1976) At Data Nucl Data Tables 17:177–210
63. Hagelaar GJM, Pitchford LC (2005) Plasma Sources Sci Technol 14:722–733
64. The Siglo Data base, CPAT and Kinema Software, http://www.siglo-kinema.com
65. Janev RK, Langer WD, Post DE Jr, Evans K Jr (1987) Elementary processes in hydrogen–helium plasmas: cross-sections and reaction rate coefficients. Springer, Berlin Heidelberg New York
66. Stevefelt J, Pouvesle JM, Bouchoule A (1982) J Chem Phys 76:4006–4015
67. Deloche R, Monchicourt P, Cheret M, Lambert F (1976) Phys Rev A 13:1140–1176
68. Rogers WA, Biondi MA (1964) Phys Rev 134:A1215–A1224
69. Herrebout D, Bogaerts A, Yan M, Gijbels R, Goedheer W, Vanhulsel A (2002) J Appl Phys 92:2290–2295
70. De Bleecker K, Bogaerts A, Goedheer W (2004) Phys Rev E 69:056409
71. Hagelaar GJM, Kroesen GMW, van Slooten U, Schreuders H (2000) J Appl Phys 88:2252–2262
72. Raizer YP, Shneider MN, Yatsenko NA (1995) Radio-frequency capacitive discharges. CRC Press, Florida
73. Schneider GE, Zedan M (1981) Numer Heat Transfer 4:1–19
74. Massines F (2001) Vide 56:55–65
75. Mangolini L, Anderson C, Heberlein J, Kortshagen U (2004) J Phys D 37:1021–1030
76. Massines F, Rabehi A, Decomps P, Gadri RB, Ségur P, Mayoux C (1998) J Appl Phys 83:2950–2957
77. Massines F, Gherardi N, Naudé N, Ségur P (2005) Plasma Phys Control Fusion 47:B577–B588
78. Massines F, Ségur P, Gherardi N, Khamphan C, Ricard A (2003) Surf Coat Technol 174:8–14
79. Golubovskii YuB, Maiorov VA, Li P, Lindmayer M (2006) J Phys D 39:1574–1583
80. Trunec D, Brablec A, Buchta J (2001) J Phys D 34:1697–1699
81. Brandenburg R, Maiorov VA, Golubovskii YuB, Wagner H-E, Behnke J, Behnke JF (2005) J Phys D 38:2187–2197
82. Bogaerts A, Gijbels R, Vlcek J (1998) J Appl Phys 84:121–136